Supplementary Appendices for "Higher-Order Topology, Monopole Nodal Lines, and the Origin of Large Fermi Arcs in Transition Metal Dichalcogenides XTe_2 (X=Mo,W)"

APPENDIX A: TIGHT-BINDING MODEL FOR FLAT-BAND HINGE STATES IN A MONOPOLE NODAL-LINE SEMIMETAL

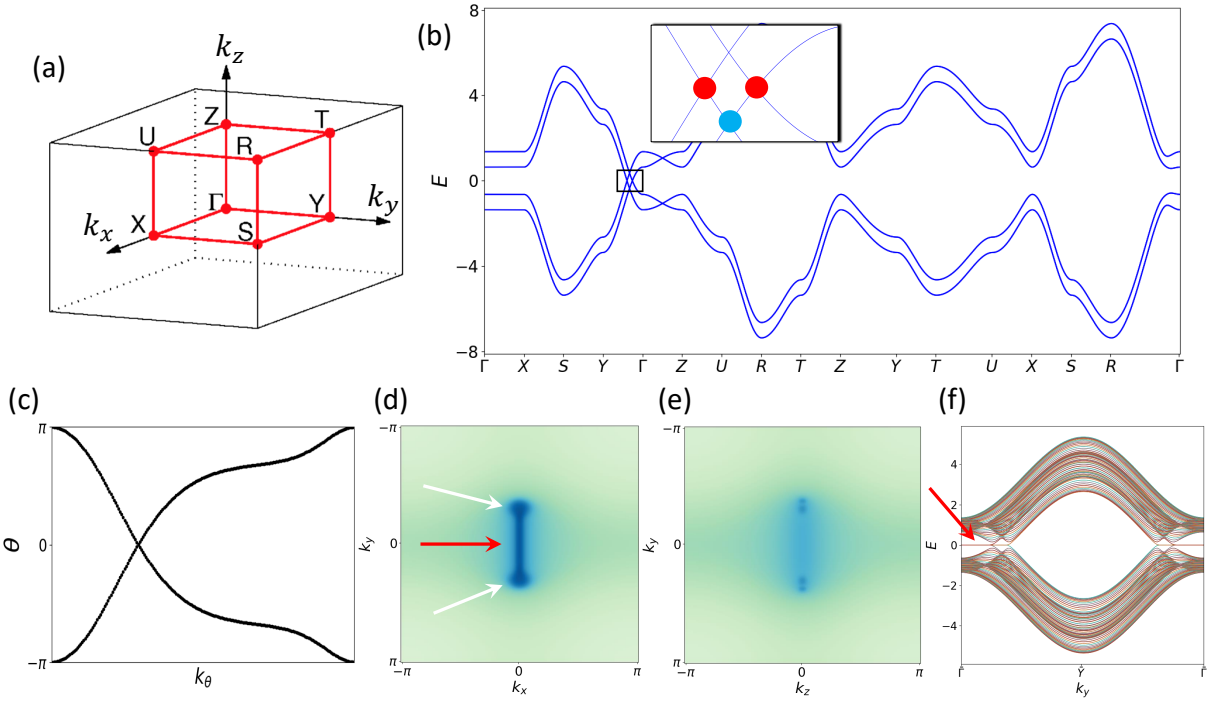

FIG. 1: (a) Primitive orthorhombic BZ[1]. (b) Bulk bands for $\tilde{\mathcal{H}}(\vec{k})$ (Eq. (A1)) with the parameters in Eq. (A3). In this limit, the eight-band model exhibits an overall $SU(2)$ spin rotation symmetry, and bands therefore appear in spin-degenerate pairs. In the inset panel, we highlight a monopole nodal line (MNL) at $E_F = 0$ along $Y\Gamma$ (red circles) that is linked to its time-reversal partner by nodal lines encircling the Γ point directly above and below E_F (blue circle) (axes not in parenthesis in Fig. 4(d)), as discussed in Ref. 2. Using the bulk tight-binding model (Eq. (A1)), we deduce that the MNLs lie in the k_{xy}-plane. (c) The Wilson loop eigenvalues over the lower four occupied bands calculated on a sphere surrounding one of the MNLs, plotted as a function of the polar momentum k_θ (Fig. 2(c) of the main text), exhibit helical winding. As detailed in Refs. 2–4, the helical winding in (c) confirms that the nodal line enclosed by the sphere carries a nontrivial monopole charge, and thus, is an MNL. (d,e) The (001) and (100) surface states of Eq. (A1), respectively, calculated at E=0. In (d), we observe both topological drumhead states on the interior projections of the bulk MNLs (white arrows)[5] and extraneous surface states (red arrows) that are remnants of the bulk double band inversion. Specifically, the interior states indicated by the white arrows are topologically protected[2], whereas the line of states shown by the red arrows is topologically trivial, and lies outside of the projections of the MNLs. The extraneous states originate from the double band inversion shown in Fig. 2: the first band inversion creates a drumhead state at $k_x = k_y = 0$ of the (001) surface BZ, and the pinching process[2] of the nodal line at half filling forms a second set of surface states, rather than removing the drumhead states from the first band inversion. The extraneous surface states are topologically trivial, and represent an artificial degeneracy in the limit of the parameters in Eq. (A3); we add the terms necessary to hybridize and gap the extra surface states in Fig. 4. (f) The bands of a z-directed slab of the model in (b), plotted at $k_x = 0$ as a function of k_y. The extraneous surface states from (d) are also marked in (f) with a red arrow.

In this section, we construct a model of a 3D nodal-line semimetal (NLSM)[5–7] that exhibits a time-reversed pair of nodal lines with nontrivial monopole charges (MNLs)[8] generated by double band inversion[2]. Using this model, we demonstrate that, when the appropriate coupling terms are added, bulk and surface gaps generically develop in the momentum-space region between the two MNLs (Fig. 4(d)). Projecting the bulk MNLs and surface drumhead states to the 1D hinges, additional 1D, flat-band-like surface states can be observed spanning the region between the projections of the MNLs. These states represent the $d-2$-dimensional generalization of drumhead surface states, and are the spinless analogs of the flat-band-like hinge states recently predicted in spinful Dirac semimetals[9,10]. In this section, we show that this monopole NLSM (MNLSM) can be gapped into either a spinless magnetic higher-order topological insulator (HOTI) (otherwise known as an "axion insulator"[2,11–15]), or into a spinful, time-reversal-

($\mathcal{T}$-) symmetric HOTI with helical pairs of hinge modes. All calculations for this section were performed employing the PythTB package[16].

To begin, we place eight spinful orbitals at the origin of a primitive orthorhombic unit cell; these can be considered four spinless orbitals (two s and two ip orbitals), each with an additional (initially uncoupled) spin-1/2 degree of freedom. We index the four pairs of spinful orbitals with the Pauli matrices τ and μ, and index the spin degree of freedom with σ. Using these orbitals, we construct the tight-binding Hamiltonian:

$$\tilde{\mathcal{H}}(\vec{k}) = \left[m_1 + \sum_{i=x,y,z} v_i \cos(k_i) \right] \tau^z + m_2 \tau^z \mu^x + m_3 \tau^z \mu^z + u_x \sin(k_x) \tau^y \mu^y + u_z \sin(k_z) \tau^x, \tag{A1}$$

which is invariant under inversion ($\mathcal{I}$) and spinless time-reversal ($\tilde{\mathcal{T}}$), represented by their action on the Hamiltonian as:

$$\tilde{\mathcal{T}} \mathcal{H}(\vec{k}) \tilde{\mathcal{T}}^{-1} = \tau^z \mathcal{H}^*(-\vec{k}) \tau^z, \; \mathcal{I} \mathcal{H}(\vec{k}) \mathcal{I}^{-1} = \tau^z \mathcal{H}(-\vec{k}) \tau^z, \tag{A2}$$

as well as, at first, $SU(2)$ spin symmetry. There are also other, extraneous symmetries, which we are free to break. For simplicity, we have chosen units in which the lattice constants $a_{x,y,z} = 1$. The representations of the symmetries in Eq. (A2) are chosen in a basis (s and ip orbitals at $(x, y, z) = (0, 0, 0)$) for which the combined antiunitary symmetry $\mathcal{I} \times \tilde{\mathcal{T}} = K$ guarantees that all of the 4×4 matrix coefficients of Eq. (A1) are real[2,8]. The form of $\tilde{\mathcal{H}}(\vec{k})$ is specifically chosen to include terms from the models in Refs. 2,8, as to guarantee that $\tilde{\mathcal{H}}(\vec{k})$ will form a pair of MNLs after undergoing double band inversion about the Γ point.

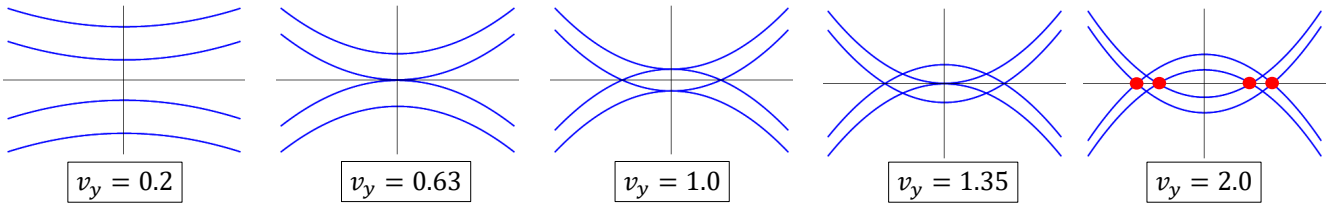

FIG. 2: Bulk bands of $\tilde{\mathcal{H}}_C(\vec{k})$ in Eq. (A10), plotted along $Y\Gamma$ in the vicinity of the Γ point with the parameters in Eqs. (A3) and varying v_y. As v_y is tuned between 0 and 2, bands become doubly inverted, and eventually form a time-reversed pair of MNLs at half filling (red circles at $v_y = 2.0$), as described in Ref. 2.

We track the bulk phase transitions of Eq. (A1) by choosing the parameters:

$$m_1 = -3, \; v_x = v_z = u_x = u_z = 1, \; m_2 = 0.3, \; m_3 = 0.2. \tag{A3}$$

and tuning v_y between 0 and 2 (Fig. 2). When $v_y \approx 0.63$, bands begin to invert at Γ, forming a nodal line (without monopole charge) between the second and third pair of spin-degenerate bands. When v_y reaches 1, the third pair of bands reaches the first pair of bands (and the second touches the fourth), and a nodal line at quarter filling (shown in blue in Fig. 4(d)) begins to form. Next, when $v_y \approx 1.35$, the nodal line at half filling begins to pinch off into a time-reversed pair of nodal lines that intersect $Y\Gamma$ (red lines in Fig. 4(d)). We then finally tune $v_y \to 2$ to grow the two nodal lines at half filling (red circles in Fig. 2) to have clearly distinguishable interior regions. Calculating the (001) and (100) surface Green's function of Eq. (A1) at $E_F = 0$ (Fig. 1(d,e)), we observe the presence of drumhead surface states (white arrows) on only the z-normal ((001)) surface, indicating that the bulk nodal lines are almost entirely normal to the k_z-axis (Fig. 4(d), axes not in parenthesis). To calculate the $\mathbb{Z}_2$ monopole charge of each nodal line, we surround it with an approximate sphere and calculate the Wilson loop eigenvalues over the lower four bands (including spin) as a function of the polar momentum (k_θ in Fig. 2(c) of the main text), as prescribed in Refs. 2–4. Most precisely, we approximate this sphere by calculating the Wilson loop on a series of concentric k_y-normal circles, indexed by k_y, and centered at $k_x = k_z = 0$, and where the radii of the circles are tapered above and below the nodal line at half filling. The Wilson loop spectrum (Figs. 1(c)) exhibits clear helical winding, confirming the nontrivial monopole charge of each nodal line at half filling[2–4].

This helical winding can be understood as reconciling the topology of the gapped planes indexed by k_y above and below the MNL. As shown in Ref. 2, the Hamiltonians of the two gapped planes are equivalent to topologically distinct 2D insulators, and can be distinguished by their (gapped) Wilson spectra. As the Wilson loop on a sphere can be deformed into the Wilson loop on the plane above the sphere minus the Wilson loop on the plane below the sphere (the prototypical explanation for the conservation of Chern number in a Weyl semimetal[17,18]), we recognize that the

gapless Wilson spectrum on the sphere reflects the Wilson loop critical point that distinguishes the 2D insulating phases above and below the MNL[2]. More precisely, Ref. 2 establishes a $\mathbb{Z}_2 \times \mathbb{Z}_2$ classification of the possible topologies of the Hamiltonians of the $\mathcal{I} \times \tilde{\mathcal{T}}$-symmetric planes above and below an MNL, and the helical winding of the sphere Wilson loop indicates a change in one of these indexes. To understand the topology of the planes with only $\mathcal{I} \times \tilde{\mathcal{T}}$ symmetry, we will first consider a topologically nontrivial 2D Hamiltonian with both $\mathcal{I}$ and $\tilde{\mathcal{T}}$ symmetry ($k_y = 0$), and will then subsequently break those symmetries in a manner that preserves their product $\mathcal{I} \times \tilde{\mathcal{T}}$ and does not close a bulk or edge (surface) gap.

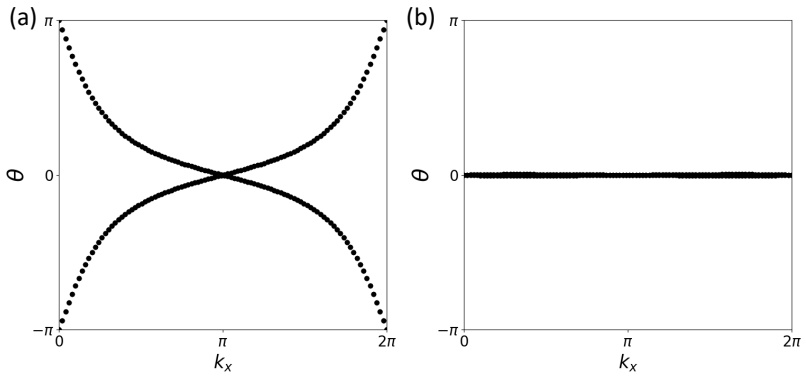

FIG. 3: (a,b) z-directed Wilson loops evaluated for the lowest two spinless pairs of bands in Fig. 1(a) at $k_y = 0, \pi$, respectively. The winding of the Wilson loop at $k_y = 0$ is not protected by spinful time-reversal symmetry, as it would be in a 2D topological insulator[19], but is instead protected by the combination of the bulk inversion eigenvalues[20] and the absence of additional bands in the Wilson projector, and thus is an example of "fragile" topology[9,14,21–24]. At $k_y = \pi$ (b), the bulk inversion eigenvalues require that $\theta = 0$ at $k_y = 0, \pi$[20]. We observe that the z-directed Wilson loop in the $k_y = \pi$ plane exhibits trivial winding, and extremely weak dispersion.

Using the results of Ref. 20, we determine that the Hamiltonian of the $k_y = 0$ plane exhibits a gapless z-directed Wilson loop with nontrivial winding (Fig. 3(a)), because all of the occupied bands have the same inversion eigenvalues at each TRIM point, and because the inversion eigenvalues at the Γ point differ from those at the three other 2D TRIM points. The winding of this Wilson loop may be removed by adding trivial bands with different inversion eigenvalues[20] (as occurs in the $k_y = 0$ plane of β-$MoTe_2$ (Fig. 3(c) of the main text)); this is a hallmark of a fragile topological phase[9,14,21–24]. Unlike in a 2D TI, we will show that the fragile Wilson loop winding at $k_y = 0$ indicates the presence of nontrivial *corner* modes. Specifically, using the $k \cdot p$ theory of Eq. (A1), we will exploit the nested Jackiw-Rebbi construction from Ref. 9, which was developed concurrently with this letter, to demonstrate that the Hamiltonian of the $k_y = 0$ plane is equivalent to a 2D insulator with gapped edges and spin-degenerate pairs of corner modes. First, we expand Eq. (A1) about the Γ point in the limit that $m_2 = m_3 = 0$, $u_x = u_z = u$:

$$\mathcal{H}_\Gamma(\vec{k}) = m\tau^z + u(\tau^y \mu^y k_x + \tau^x k_z), \tag{A4}$$

where we have condensed all of the terms proportional to τ^z into a single mass term m. We then take m to vary spatially, such that it is negative in a circular region bound by a radius R and large and positive outside of it. The bound state solutions on the exterior of this region can be obtained by forming a Jackiw-Rebbi domain wall[25] at $r = R$, which we accomplish by Fourier transforming $k_{x,z} \to -i\partial_{x,z}$ and converting to polar coordinates:

$$\mathcal{H}(r, \theta) = m(r)\tau^z - iu\Gamma^1(\theta)\partial_r - \frac{iu}{r}\Gamma^2(\theta)\partial_\theta, \tag{A5}$$

where:

$$\Gamma^1(\theta) = \tau^x \cos(\theta) + \tau^y \mu^y \sin(\theta),\ \Gamma^2(\theta) = -\tau^x \sin(\theta) + \tau^y \mu^y \cos(\theta). \tag{A6}$$

In the absence of additional terms, $\mathcal{H}(r, \theta)$ exhibits gapless, linear dispersing modes on its edges, as in this limit it is closely related to the $k \cdot p$ theory of a 2D topological insulator[9,19]. More specifically, despite having only spinless time-reversal symmetry, $\mathcal{H}(r, \theta)$ still exhibits linear dispersion with three anticommuting 4×4 Dirac matrices, like the $k \cdot p$ theory of the Bernevig-Hughes-Zhang model of a 2D TI[9,19]. In polar coordinates, the symmetries of $\mathcal{H}(r, \theta)$ are represented by their action:

$$\tilde{\mathcal{T}}\mathcal{H}(r, \theta)\tilde{\mathcal{T}}^{-1} = \tau^z \mathcal{H}^*(r, \theta)\tau^z,\ \mathcal{I}\mathcal{H}(r, \theta)\mathcal{I}^{-1} = \tau^z \mathcal{H}(r, \theta + \pi)\tau^z. \tag{A7}$$

The symmetries in Eq. (A7) permit a set of bulk mass terms that includes:

$$V_L(\theta) = \tau^y \mu^x \sin(L\theta + \phi),\ L = L^{FTI} = 1 + 2n,\ n \in \mathbb{Z}, \tag{A8}$$

where $V_L(\theta)$ anticommutes with all of the existing terms in $\mathcal{H}(r,\theta)$, and is therefore guaranteed to open bulk (and edge) gaps in all of the regions in which it is nonzero. We use the label "FTI" on L in Eq. (A8) to emphasize that $V_L(\theta)$ is the intrinsic bulk mass of a fragile TI. In Eq. (A8), the integer L is the "angular momentum" of the mass term[9], and ϕ is a free angle. When L takes its lowest symmetry-allowed value ($L = L^{FTI} = 1$), $V_L(\theta)$ becomes proportional to the circular harmonic[9] of a p orbital lying in the xz-plane whose lobes are oriented at an angle ϕ from the x axis. The Hamiltonian $\mathcal{H}(r,\theta) + V_L(\theta)$ therefore exhibits $2L = 2 + 4n$ spin-degenerate pairs of 0D bound states, where each pair of bound states at θ is related by $\mathcal{I}$-symmetry to a second pair at $\theta + \pi$ (see Ref. 9 for a more explicit derivation of the form of these 0D states and the role of curvature in this geometry). Other mass terms are also allowed; however, in the 4×4 basis of $\tau^i \otimes \mu^i$, all $\mathcal{I}$-symmetric bulk mass terms that anticommute with τ^z will necessarily also carry a spatial distribution $\sin(L^{FTI}\theta + \phi)$. This indicates that the number of spin-degenerate pairs of 0D boundary modes modulo 4 is an intrinsic property of $\mathcal{H}(r,\theta)$, with the smallest number (and the number seen in our numerics (Fig. 4(f)) being 2. We therefore conclude that the $k_y = 0$ plane of Eq. (A1) is an additional example of a "fragile" topological phase[9,14,21–24] that exhibits anomalous corner modes[9,14] on the boundary of a finite-sized region with inversion symmetry. Furthermore, at half-filling, each pair of 0D states exhibits a charge $\pm e/2$ per spin[9,14], where, specifically, $\mathcal{I}$-related bound states exhibit opposite charges[14] within each spin sector indexed by σ^z. As discussed in Ref. 9, this can be reformulated as the statement that the boundary of $\mathcal{H}(r,\theta) + V_L(\theta)$ exhibits a set of 0D charges with a total dipole moment per spin given by the sum of $L^{FTI} = 1 + 2n$ free-angle dipoles, where each dipole has the same magnitude of $e/2$ per unit length . Therefore, as first noted in Ref. 9, Eqs. (A5) and (A8) bear similarities with recent gauge-theory descriptions of fractons with anomalous "vector" charges[26].

We can model the process of moving to nearby planes indexed by $k_y \neq 0$ by considering the effect of introducing a bulk (spinless) mass term to Eqs. (A5) and (A8) that breaks $\mathcal{I}$ and $\tilde{\mathcal{T}}$ while preserving their product. As we are still preserving $SU(2)$ spin symmetry, any additional term that does not close the bulk or edge gaps can only act as an $\mathcal{I} \times \tilde{\mathcal{T}}$-symmetric chemical potential on the corner modes[9]. As previously shown, the two midgap corner modes at $k_y = 0$ of the $L = 1$ term in Eq. (A8) are related by $\mathcal{I}$ symmetry, and therefore remain anomalous if $\mathcal{I}$ is relaxed while preserving the combined operation $\mathcal{I} \times \tilde{\mathcal{T}}$. When extra (trivial) bands without corner modes are added to remove the Wilson-loop winding, the $k_y = 0$ plane of Eq. (A1) should exhibit a gapped Wilson spectrum with the same $\mathbb{Z}_2$-quantized nested Berry phase as the $k_y = 0$ plane of β-$MoTe_2$ (Fig. 3(c) of the main text and Appendix B 3, confirmed by explicit calculation in Ref. 14 after the submission of this letter). Therefore, when a bulk term is added that preserves $\mathcal{I} \times \tilde{\mathcal{T}}$ while breaking the individual symmetries $\mathcal{I}$ and $\tilde{\mathcal{T}}$, the nested Berry phase will *remain* quantized and the corner modes will remain present. This indicates that, as all of the Hamiltonians of the k_y-indexed planes between the MNLs in our tight-binding model can be connected to the Hamiltonian of the plane at $k_y = 0$ without closing a bulk or edge gap, they should also carry corner (hinge) modes indicated by a quantized nested Berry phase $\gamma_2 = \pi$. Utilizing the Wannier description of corner-mode phases developed in Ref. 9, this suggests that the four possible insulating phases of the Hamiltonians of the $\mathcal{I} \times \tilde{\mathcal{T}}$-symmetric $k_y \neq 0$ planes between the MNLs in Eq. (A1), which were determined in Ref. 2 to have a $\mathbb{Z}_2 \times \mathbb{Z}_2$ topological classification, correspond to either *non-symmetry-indicated* obstructed atomic limits[27] or trivialized fragile topological insulators (for a large number of occupied bands)[9,14,21–24] that differ by the number of Wannier orbitals on each of the four $\mathcal{I} \times \tilde{\mathcal{T}}$ centers of magnetic layer group $p\bar{1}'$[9,28]. After the submission of this letter, this Wannier description of $\mathcal{I} \times \tilde{\mathcal{T}}$- (or $C_2 \times \mathcal{T}$-) symmetric (trivialized) fragile phases with corner modes was subsequently confirmed and expanded in Refs. 14,15,29–31.

To detect the hinge states implied by Eqs. (A5) and (A8) and the surrounding text, we must formulate a tight-binding model without the extraneous surface drumhead states shown with red arrows in Fig. 1(d,f), such that there is a projected bulk and surface gap in the spectrum of a y-directed rod[9]. We first examine the extraneous surface spectral weight in Fig. 1(d) more closely by calculating the bands of a z-directed slab of $\tilde{\mathcal{H}}(\vec{k})$ with the parameters listed in Eq. (A3) (Fig. 1(f)). We observe that the process of double band inversion has, in addition to nucleating the expected drumhead states in the interior projections of the MNLs (Fig. 1(d), white arrows), left behind a trivial pair of drumhead states[5–7] where the nodal line at half filling was pinched and split (Fig. 1(d,f), red arrows). As there is no surface wallpaper group symmetry[39,40] that protects the overlap of the extra surface states, we are free to add a bulk term that couples and gaps the trivial drumheads, analogous to the coupling that is naturally present in β-$MoTe_2$ (Fig. 4 of the main text). We therefore introduce the bulk term:

$$\tilde{V}(\vec{k}) = m_{v1}\mu^z + m_{v2}\mu^x, \tag{A9}$$

realizing the coupled Hamiltonian:

$$\tilde{\mathcal{H}}_C(\vec{k}) = \tilde{\mathcal{H}}(\vec{k}) + \tilde{V}(\vec{k}). \tag{A10}$$

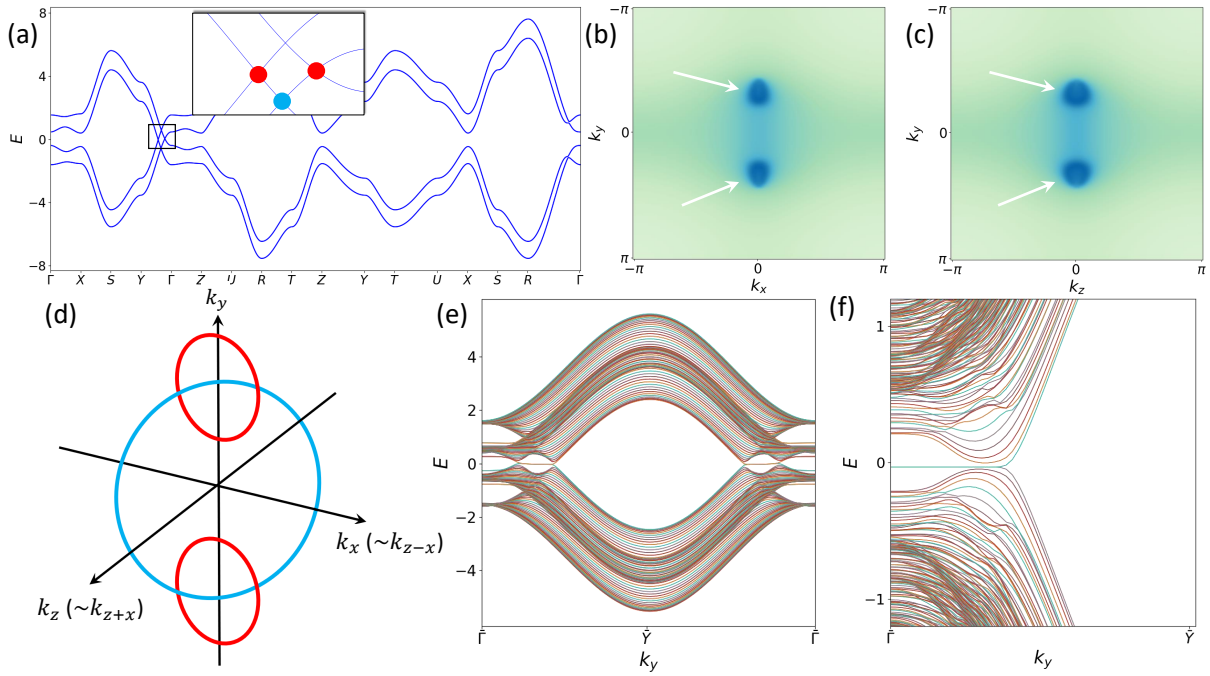

FIG. 4: (a) Bulk bands for $\tilde{\mathcal{H}}_C(\vec{k})$ in Eq. (A10), plotted with the parameters in Eqs. (A3) and (A11). (b,c) (001) and (100) surface Green's function at $E_F = 0$ for the same model, respectively. Topological drumhead states appear on both surfaces in the interior projections of the MNLs (white arrows), indicating that the MNLs have become tilted and now have nonzero projections in both the x and z directions. Crucially, the extraneous surface spectral weight spanning the projections of the MNLs from Fig. 1(d) has been lifted. (d) Specifically, we observe that both the nodal lines at half filling (red), and the large nodal line directly below it in energy (blue) have become tilted by $\sim 45^\circ$ about the k_y axis (axes in parenthesis are those after including Eq. (A10)). (e) The bands of a z-directed slab of $\tilde{\mathcal{H}}_C(\vec{k})$, plotted at $k_x = 0$ as a function of k_y, confirm that the extra surface states have hybridized and split. (f) The bands of a y-directed rod of $\tilde{\mathcal{H}}_C(\vec{k})$ (finite in the x and z directions). Flat-band-like 1D states can be observed spanning the hinge projections of the MNLs; these are the spinless, $\mathcal{I} \times \tilde{\mathcal{T}}$-protected analogs of the hinge states recently predicted in spinful Dirac semimetals[9,10].

Choosing the parameters:

$$m_{v1} = -0.4, \; m_{v2} = 0.2, \tag{A11}$$

in addition to those listed in Eq. (A3), we again plot the bulk bands, (001) surface Green's function, (100) surface Green's function, and the z-directed slab bands at $k_x = 0$ (Fig. 4(a,b,c,e)). We observe that drumhead states now appear on both the (001) and (100) surfaces (Fig. 4(b,c), white arrows), indicating that the bulk MNLs have become tilted (Fig. 4(d)), and now carry nonzero interior projections in both the x and z directions. Crucially, in the region between the surface projections of the bulk MNLs, the two extraneous drumhead states have become hybridized and split by the new mass terms in Eq. (A9).

Following the procedure employed in Ref. 9, we construct a y-directed rod of $\tilde{\mathcal{H}}_C(\vec{k})$, *i.e.*, a tight-binding model that is finite in the x and z directions and infinite in the y direction. To understand the bulk and surface states that project to the hinges, one can take Fig. 4(b) and then project all of the surface spectral weight to the k_y axis; the region between the two drumhead states (centered on the projection of Γ) remains free of surface (and bulk) states. Plotting the hinge states of this rod (Fig. 4(f)), additional, 1D flat-band-like states are visible spanning the hinge projections of the MNLs. Specifically, at each value of k_y along the rod between the projections of the MNLs, there are four additional hinge states, which appear in spin-degenerate pairs localized on opposing hinges (Fig. 5(c)). These hinge states represent the $d-2$-dimensional generalization of the drumhead surface states of nodal-line semimetals[5–7], and are the spinless analogs of the hinge states recently proposed in spinful Dirac semimetals[9,10]. It is clear that the k_y-indexed planes that exhibit hinge states in Fig. 4(f) lack the fourfold rotation and reflection symmetries of previously identified semimetals with hinge states[9,10].

In light of the relationship between MNLs and higher-order topology explored in the main text, we recognize the hinge states in Fig. 4(f) as the spinless precursors to the spinful helical hinge modes of 3D HOTIs. They represent the higher-order generalization of the zigzag edge states of graphene[41–45], which analogously evolve into the helical

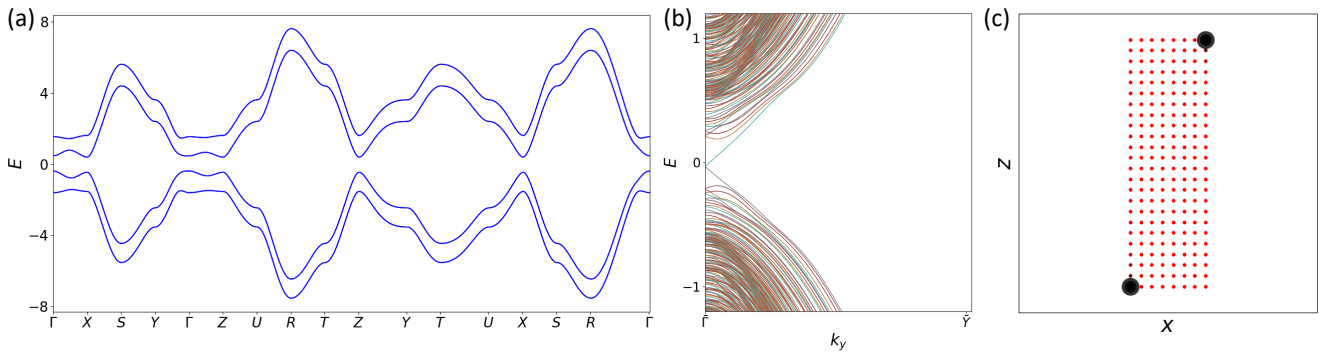

FIG. 5: (a) Bulk and (b) hinge bands of a y-directed rod of $\tilde{\mathcal{H}}_C(\vec{k})$ (Eq. (A10)) with the Kane-Mele-like SOC term $V_{HOTI}(\vec{k})$ (Eq. (A13)), plotted with the parameters in Eqs. (A3) and (A11) and $v_H = 1.2$. The flat-band hinge states from Fig. 4(f) have evolved into a pair of 1D helical modes. (c) The localization in the xz-plane of the hinge states at $k_y = 0$; the two helical pairs of hinge modes are localized on $\mathcal{I}$-related hinges, confirming that $V_H(\vec{k})$ induces a phase transition from an MNL semimetal to an $\mathcal{I}$- and $\mathcal{T}$-symmetric HOTI[14,32–38]. When $V_{Axion}(\vec{k})$ (Eq. (A12)) is used instead of $V_{HOTI}(\vec{k})$), the bulk bands appear similar to those in (a), but the hinge spectrum instead exhibits oppositely propagating spin-degenerate pairs of chiral modes on $\mathcal{I}$-related hinges; this magnetic insulator is the spinless analog of the axion insulators analyzed in Refs. 13–15.

edge modes of a 2D TI[46,47] under the introduction of SOC. As the MNLs are locally protected by $\mathcal{I}$, $\tilde{\mathcal{T}}$, and $SU(2)$ spin symmetry[5,8], we can realize a bulk-insulating phase by relaxing one of these symmetries. First, we reproduce the results of Ref. 2 by introducing a term that breaks $\tilde{\mathcal{T}}$ symmetry while preserving $\mathcal{I}$ and $SU(2)$:

$$V_{Axion}(\vec{k}) = v_A \sin(k_y)\tau^y\mu^z. \tag{A12}$$

We observe that $V_{Axion}(\vec{k})$ fully gaps the bulk and surface bands, realizing an insulating phase with spin-degenerate, chiral hinge modes (the bulk and hinge bands appear qualitatively similar to those shown in Fig. 5, as bands of opposite chirality from opposing hinges become projected on top of each other). Eq. (A12) is therefore the higher-order analog of the magnetic Haldane term that gaps graphene into a spinless Chern insulator[48]. We recognize the gapped 3D phase induced by $V_{Axion}(\vec{k})$ as the magnetic HOTI that results from gapping all of the surfaces of a 3D strong TI with magnetism that is spatially distributed in an $\mathcal{I}$-odd fashion[11,13,14,37]. It is therefore also equivalent to two, spin-degenerate copies of a spinful axion insulator[2,14] that are prevented from trivially hybridizing by $SU(2)$ symmetry.

Finally, we can also introduce a term of a similar form:

$$V_{HOTI}(\vec{k}) = v_H \sin(k_y)\tau^y\mu^z\sigma^z, \tag{A13}$$

that breaks spinless time-reversal symmetry $\tilde{\mathcal{T}}$ and $SU(2)$ symmetry while preserving *spinful* $\mathcal{T}$ symmetry, which is represented by the action:

$$\mathcal{T}\mathcal{H}(\vec{k})\mathcal{T}^{-1} = (i\sigma^y\tilde{\mathcal{T}})\mathcal{H}(\vec{k})(i\sigma^y\tilde{\mathcal{T}})^{-1} = \sigma^y\tau^z\mathcal{H}^*(-\vec{k})\sigma^y\tau^z. \tag{A14}$$

V_{HOTI} term gaps the bulk MNLs (Fig. 5(a)) and opens up the spin-degenerate flat-band hinge states (Fig. 4(e)) into the helical hinge modes of a HOTI. Eq. (A13) is therefore the higher-order analog of the Kane-Mele SOC term that gaps graphene into a 2D TI[46,47]. Thus, we have demonstrated that double band inversion in an $\mathcal{I}$- and $\mathcal{T}$-symmetric crystal with vanishing SOC can induce a pair of MNLs, which in turn can be gapped with $\mathcal{I}$-symmetric SOC to realize a $\mathbb{Z}_4$-nontrivial HOTI[35–38].

We note that, unlike $MoTe_2$ (Fig. 4(d,e) of the main text and Fig. 6(e,f) in Appendix B 4), the HOTI induced by Eq. (A13) *does not* display large gapped surface Fermi arcs at low energies. Instead, its bulk and surfaces are fully insulating (Fig. 5(b)). However, if parameters were adjusted to give greater dispersion to the gapped drumhead states near $\bar{\Gamma}$ in Fig. 4(e), then, in the presence of SOC (Eq. (A13)), the surface Green's functions in Fig. 4(b,c) would begin to exhibit pairs of arc-like states from gapped surface Dirac cones, like those in $MoTe_2$. This reinforces the notion that, in d-dimensional insulators with higher-order topological boundary modes, the $d-1$-dimensional gapped surface states, while still topological (in the sense that they represent of anomalous "halves" of isolated $d-1$-dimensional topological (crystalline) insulators[9,14,39,49–52]), can nevertheless be moved away from the Fermi energy (and possibly into the bulk manifolds) without breaking a symmetry or closing a bulk or surface gap.

APPENDIX B: FIRST-PRINCIPLES CALCULATIONS DETAILS

1. Density Functional Theory Calculation Methods

First-principles electronic structure calculations were performed with the projector augmented wave (PAW) method[53,54] as implemented in the VASP package[55,56]. We adopted the Perdew-Burke-Ernzerhof (PBE) generalized gradient approximation (GGA) for the exchange-correlation functional[57]. SOC was incorporated self-consistently. The kinetic energy cutoff of the plane-wave basis was set to 400 eV. A 6×12×4 k-point mesh was employed for BZ sampling. Internal atomic positions and cell parameters were obtained from experimental data for β-$MoTe_2$ in space group 11 $P2_1/m$ (ICSD[58] #14349)[59]. The maximally localized Wannier functions (MLWF) were constructed from first-principles calculations[60] using the d orbitals of Mo and the p orbitals of Te. The Wannier-based tight-binding Hamiltonian obtained from this construction was used to compute the surface spectrum and the nested Wilson loop[49,61,62] matrix $W_2(k_y)$ as described in Appendix B 3.

2. First-Principles Calculation of Monopole Charge

When the effects of SOC are neglected, the electronic structure of β-$MoTe_2$ exhibits two nodal lines connecting the 28$^{\text{th}}$ and 29$^{\text{th}}$ spin-degenerate pair of bands, related by inversion symmetry, lying on either side of the $k_y = 0$ plane, and intersecting $Y\Gamma$ (Fig. 2(b) of the main text). Rather than surround one of these nodal lines with a sphere, as is done in Refs. 2–4 for tight-binding models, we surround it with a geometrically simpler closed tetragonal prism. Defining the Wilson matrix as the product of the adjacent overlap matrices – $\langle u_{\mathbf{k}_1}|u_{\mathbf{k}_2}\rangle$ –, where $|u_{\mathbf{k}}\rangle$ is the cell-periodic part of the Bloch eigenstate, we calculate the phases of the Wilson loop eigenvalues over the lower 28 spin-degenerate pairs of bands on the following paths along this prism, shown in Fig. 2(c) of the main text. We begin by calculating the loops on the bottom of the prism along the path $(x, 0, x) \to (-x, 0, x) \to (-x, 0, -x) \to (x, 0, -x) \to (x, 0, x)$, taking x to vary from 0 to 0.45 in units of the reciprocal lattice vectors. We choose the bound $x = 0.45$ such that the prism can contain as much as possible of the half BZ without touching the zone edge. We then take loops of increasing height y along the sides of the prism along the path $(0.45, y, 0.45) \to (-0.45, y, 0.45) \to (-0.45, 0, -0.45) \to (0.45, 0, -0.45) \to (0.45, 0, 0.45)$, taking y to vary from 0 to 0.5. We finally close the exterior of the prism by taking square loops on the top of decreasing width $2x$, where each loop is taken along the path $(x, 0.5, x) \to (-x, 0.5, x) \to (-x, 0.5, -x) \to (x, 0.5, -x) \to (x, 0.5, x)$, taking x to vary from 0.45 to 0. We plot in the inset panel of Fig. 2(b) of the main text the resulting Wilson spectrum as a function of x for the bottom, then y for the sides, and then finally $-x$ for the top, which we condense and label as the overall "polar momentum" k_θ. The Wilson loop eigenvalues exhibit the characteristic winding of an MNL (Appendix A)[2–4].

3. Calculating the Wilson Loop of the Wilson Loop and Quantization of the Nested Berry Phase

Here, we detail the calculations performed to obtain the determinant of the nested Wilson loop matrix $W_2(k_y)$ (defined rigorously in Appendix B 3 a) in Fig. 3 of the main text. We first, neglecting the effects of SOC, calculate the k_z-directed Wilson loop matrix $W_1(k_x, k_y)$ over the lower 28 spin-degenerate pairs of bands, which can be expressed as $\langle u^0|u^N\rangle \langle u^N|u^{N-1}\rangle \dots \langle u^1|u^0\rangle$, where N is the discretized N-th k point of the line: $(k_x, k_y, 0) \to (k_x, k_y, 2\pi)$. Diagonalizing the resulting Wilson loop matrix, we obtain the eigenvectors $|\tilde{u}^n(k_x, k_y)\rangle$ and eigenvalues $\xi_1^n(k_x, k_y)$ as functions of (k_x, k_y), where n is the Wilson band index. The eigenvalues $\xi_1^n(k_x, k_y)$ appear in the form $e^{i\theta_1^n(k_x,k_y)}$. In Fig. 3(c,d) of the main text, we show the calculated values of $\theta_1^n(k_x, 0)$ and $\theta_1^n(k_x, \pi)$, respectively, which we refer to as the Wilson bands. In all of the k_y-indexed planes away from the MNLs, the Wilson bands are well separated by gaps in the Wilson spectrum at $\theta_1 = \pm\pi/2$ ($0.25 \times (2\pi)$, as expressed in the main text). The system $H_{W_1}(k_x, k_y) \equiv \sum_{|\theta_1^n|<(\pi/2)} |\tilde{u}^n(k_x, k_y)\rangle\, \theta_1^n(k_x, k_y)\, \langle\tilde{u}^n(k_x, k_y)|$ resembles a 1D periodic Hamiltonian for fixed values of k_y, and its eigenstates can be used to calculate a second, nested Wilson loop matrix $W_2(k_y)$ whose determinant is equal to $e^{i\gamma_2(k_y)}$, where $\gamma_2(k_y)$ is the nested Berry phase[14,49,61,62] of each plane indexed by k_y. We compute the determinant of $W_2(k_y)$ for all values of k_y, and observe that it is quantized at ± 1 for all values of k_y away from the MNLs, and jumps as the plane on which it is calculated passes fully over an MNL (Fig. 3(b) of the main text).

a. Nested Berry Phase Quantization from $\mathcal{I}\times\mathcal{T}$ Symmetry

We note that the choice of Wilson energy interval employed for the nested Wilson loop calculations in this letter is different than that used in previous works[9,61,62]. Specifically, in previous works, the Wilson spectrum was divided into halves between $\theta_1 = 0, \pi$ for nested Wilson loop calculations; here, we instead choose the particle-hole-symmetric interval $\theta_1 \in [-\pi/2, \pi/2)$. However, as long as the nested Wilson loop (and Berry phase) is calculated over the same Wilson interval for two different 2D insulators (or planes of the BZ), it can be used as a tool to compare their topology[61].

Furthermore, we discover in this letter that when the nested Berry phase γ_2 is calculated over this new choice of Wilson energies, it can be quantized without relying on mirror and fourfold rotation, as was previously required to quantize the nested Berry phase of the quadrupole insulators in Refs. 9,61. In this section, we will show that, in particular, the combined antiunitary symmetry $\mathcal{I}\times\mathcal{T}$ is sufficient to quantize γ_2 when W_2 is calculated over a particle-hole symmetric set of Wilson bands. We will find that a set of Wilson bands with quantized γ_2 does not need to lie specifically within the Wilson energy range employed in this letter ($\theta_1 \in [-\pi/2, \pi/2)$), or even be contiguous in Wilson energy[14]; the only restriction is that the set of Wilson bands within the nested Wilson projector returns to itself under the action of a Wilson particle-hole-symmetry that originates from bulk $\mathcal{I}\times\mathcal{T}$ symmetry. The existence of this particle-hole symmetry in the Wilson spectrum was first derived in Ref. 20; we reproduce its derivation here for convenience, and then use the result to demonstrate the $\mathbb{Z}_2$ quantization of γ_2.

To begin, we first consider a 3D orthorhombic crystal with a bulk Hamiltonian $\mathcal{H}(k_x, k_y, k_z)$ that is invariant under $\mathcal{I}\times\mathcal{T}$, where $\mathcal{T}$ can represent either spinless ($\mathcal{T}^2 = +1$) or spinful ($\mathcal{T}^2 = -1$) time-reversal. We then calculate the discretized z-directed Wilson loop as it is defined in Refs. 20,39,63:

$$\begin{aligned}\left[W_{1(k_\perp,k_{z0})}\right]_{nm} &\equiv \left[\mathcal{P}e^{i\int_{k_{z0}}^{k_{z0}+2\pi} dk_z A_z(k_\perp,k_{z0})}\right]_{nm}\\ &\approx \left[\mathcal{P}e^{i\frac{2\pi}{N}\sum_{j=1}^{N} A_z(k_\perp,k_{z0}+\frac{2\pi j}{N})}\right]_{nm}\\ \approx \langle u^n(k_\perp,k_{z0}+2\pi)|\Bigg[\mathcal{P}\prod_{j=1}^{N} P(k_\perp,k_{z0}+\frac{2\pi j}{N})&\left(1-\frac{2\pi}{N}\partial_{k_z}|_{(k_\perp,k_{z0}+\frac{2\pi j}{N})}\right)P(k_\perp,k_{z0}+\frac{2\pi j}{N})\Bigg]|u^m(k_\perp,k_{z0})\rangle\\ &\approx \langle u^n(k_\perp,k_{z0})|V(2\pi\hat{z})\Pi(k_\perp,k_{z0})|u^m(k_\perp,k_{z0})\rangle, \end{aligned} \tag{B1}$$

where $k_\perp \equiv (k_x, k_y)$, $P(\mathbf{k})$ is the projector onto the occupied states (here the separated grouping of energy bands):

$$P(\mathbf{k}) = \sum_{n=1}^{n_{\text{occ}}} |u^n(\mathbf{k})\rangle\langle u^n(\mathbf{k})|, \tag{B2}$$

and where in the last line of Eq. (B1), we have defined the ordered product of projectors,

$$\Pi(k_\perp, k_{z0}) \equiv P(k_\perp, k_{z0}+2\pi)P(k_\perp, k_{z0}+\frac{2\pi(N-1)}{N})\cdots P(k_\perp, k_{z0}+\frac{2\pi}{N}). \tag{B3}$$

The discretized loop defined by the product of projectors in Eq. (B1) is closed by a sewing matrix:

$$[V(2\pi\hat{z})]_{nm} = |u^n(k_\perp, k_{z0})\rangle\langle u^m(k_\perp, k_{z0}+2\pi)|, \tag{B4}$$

that enforces the gauge and basepoint (k_{z0}) invariance of the eigenvalues of Eq. (B1)[20,39,63]. We then define a Hermitian "Wilson Hamiltonian,"

$$\left[H_{W_{1(k_{z0})}}(k_x,k_y)\right]_{nm} = \left[-i\ln(W_{1(k_x,k_y,k_{z0})})\right]_{nm} \equiv H_{W_1}(k_x,k_y) = -i\ln(W_1(k_x,k_y)), \tag{B5}$$

where in the equivalence we define the less formal expressions for the z-directed Wilson Hamiltonian and loop with suppressed band indices used throughout this letter.

From the analysis provided in Refs. 39,63, we recognize that the bulk symmetry $\mathcal{I}\times\mathcal{T}$ acts on $H_{W_1}(k_x, k_y)$ as an antiunitary particle-hole symmetry $\tilde{\Xi}$, but one that does not change the signs of $k_{x,y}$. Specifically, because $\mathcal{I}\times\mathcal{T}$ does not change the direction of the product of projectors in Eq. (B1), the action of $\mathcal{I}\times\mathcal{T}$ on $W_1(k_x, k_y)$ can simply be deduced from Eqs. (B2) and (B4):

$$\begin{aligned}(\mathcal{I}\times\mathcal{T})W_{1(k_x,k_y,k_{z0})}(\mathcal{I}\times\mathcal{T})^{-1} &= (\mathcal{I}\times\mathcal{T})V(2\pi\hat{z})\Pi(k_x,k_y,k_{z0})(\mathcal{I}\times\mathcal{T})^{-1}\\ &= UV^*(2\pi\hat{z})\Pi^*(k_x,k_y,k_{z0})U^\dagger\\ &= UW^*_{1(k_x,k_y,k_{z0})}U^\dagger, \end{aligned} \tag{B6}$$

where $[U, W^*_{1(k_x,k_y,k_{z0})}] = 0$ for spinless electrons. The Wilson Hamiltonian is therefore invariant under an antiunitary particle-hole symmetry, which we denote as $\tilde{\Xi}$, that leaves $k_{x,y}$ invariant:

$$\tilde{\Xi} H_{W_1}(k_x, k_y)\tilde{\Xi}^{-1} = -\tilde{U}(k_x, k_y) H^*_{W_1}(k_x, k_y)\tilde{U}^\dagger(k_x, k_y), \tag{B7}$$

for which one can choose $\tilde{U}(k_x, k_y) = \mathbb{1}$ for spinless electrons without loss of generality. Eq. (B7) implies that for every Wilson eigenstate $|\tilde{u}^n(k_x, k_y, k_{z0})\rangle$ with eigenvalue $\theta_1^n(k_x, k_y)$, there is another eigenstate with eigenvalue $-\theta_1^n(k_x, k_y)$:

$$\tilde{\Xi}|\tilde{u}^n(k_x, k_y, k_{z0})\rangle = \tilde{U}'(k_x, k_y, k_{z0})(|\tilde{u}^n(k_x, k_y, k_{z0})\rangle)^*, \tag{B8}$$

where $\tilde{U}'(k_x, k_y, k_{z0})$ is the product of $\tilde{U}(k_x, k_y)$ in Eq. (B7) and a $\mathbf{k}$-dependent unitary transformation that rotates the Wilson band index n, and is present for both spinful and spinless electrons.

As $H_{W_1}(k_x, k_y)$ is well-defined and generically gapped in the momentum-space regions for which $\mathcal{H}(k_x, k_y, k_z)$ is gapped (for a sufficiently large number of occupied bands (Refs. 2,20 and Appendix A)), we can calculate the x-directed nested Wilson matrix $W_2(k_y)$ by projecting onto half of the eigenstates of $H_{W_1}(k_x, k_y)$ and repeating the Wilson loop calculation in Eq. (B1). Formally, we define the x-directed nested Wilson loop:

$$\begin{aligned}
\left[W_{2(k_{x0},k_y,k_{z0})}\right]_{nm} &\equiv \left[\mathcal{P} e^{i\int_{k_{x0}}^{k_{x0}+2\pi} dk_x \tilde{A}_x(k_{x0},k_y,k_{z0})}\right]_{nm} \\
&\approx \left[\mathcal{P} e^{i\frac{2\pi}{N}\sum_{j=1}^{N} \tilde{A}_x(k_{x0}+\frac{2\pi j}{N},k_y,k_{z0})}\right]_{nm} \\
\approx \langle \tilde{u}^n(k_{x0}+2\pi, k_y, k_{z0})| \Bigg[\mathcal{P}\prod_{j=1}^{N} \tilde{P}(k_{x0}+\frac{2\pi j}{N}, k_y, k_{z0}) &\left(1 - \frac{2\pi}{N}\partial_{k_x}|_{k_{x0}+\frac{2\pi j}{N},k_y,k_{z0})}\right) \tilde{P}(k_{x0}+\frac{2\pi j}{N}, k_y, k_{z0})\Bigg] |\tilde{u}^m(k_{x0}, k_y, k_{z0})\rangle \\
&\approx \langle \tilde{u}^n(k_{x0}, k_y, k_{z0})|\tilde{V}(2\pi\hat{x})\tilde{\Pi}(k_{x0}, k_y, k_{z0})|\tilde{u}^m(k_{x0}, k_y, k_{z0})\rangle,
\end{aligned} \tag{B9}$$

where tildes indicate quantities obtained from the Wilson Hamiltonian (Eq. (B5)), $\tilde{P}(\mathbf{k})$ is the projector onto the occupied Wilson states (here the separated grouping of Wilson bands):

$$\tilde{P}(\mathbf{k}) = \sum_{n=1}^{\tilde{n}_{\text{occ}}} |\tilde{u}^n(\mathbf{k})\rangle\langle\tilde{u}^n(\mathbf{k})|, \tag{B10}$$

and where in the last line of Eq. (B9), we have defined the ordered product of Wilson projectors,

$$\tilde{\Pi}(k_{x0}, k_y, k_{z0}) \equiv \tilde{P}(k_{x0}+2\pi, k_y, k_{z0})\tilde{P}(k_{x0}+\frac{2\pi(N-1)}{N}, k_y, k_{z0})\cdots\tilde{P}(k_{x0}+\frac{2\pi}{N}, k_y, k_{z0}). \tag{B11}$$

The discretized nested loop in Eq. (B9) is also closed by a sewing matrix:

$$\left[\tilde{V}(2\pi\hat{x})\right]_{nm} = |\tilde{u}^n(k_{x0}, k_y, k_{z0})\rangle\langle\tilde{u}^m(k_{x0}+2\pi, k_y, k_{z0})|, \tag{B12}$$

that enforces the basepoint (k_{x0}) independence of Eq. (B9)[61,62] in the same manner that Eq. (B4) does for Eq. (B1). The eigenvalues of $W_{2(k_{x0},k_y,k_{z0})}$ are gauge-independent[61,62] and take the form of phases $\exp(i\theta_2(k_y))$. We can thus define a Hermitian "nested Wilson Hamiltonian,"

$$\left[H_{W_{2(k_{x0},k_{z0})}}(k_y)\right]_{nm} = \left[-i\ln(W_{2(k_{x0},k_y,k_{z0})})\right]_{nm} \equiv H_{W_2}(k_y) = -i\ln(W_2(k_y)), \tag{B13}$$

where in the equivalence, we define the less formal expressions for the x-directed nested Wilson Hamiltonian and loop with suppressed Wilson band indices used throughout this letter. The eigenvalues of $H_{W_{2(k_{x0},k_{z0})}}(k_y)$ take the form of real angles $\theta_2(k_y)$, and we refer to the values of $\theta_2(k_y)$ as "nested Wilson energies." At each value of k_y, the sum of the nested Wilson energies modulo 2π is equal to the nested Berry phase:

$$\gamma_2(k_y) = \sum_{n=1}^{\tilde{n}_{\text{occ}}} \theta_2^n(k_y) \bmod 2\pi. \tag{B14}$$

We can now determine the action of $\tilde{\Xi}$ (and thus $\mathcal{I}\times\mathcal{T}$) on the nested Wilson loop. Crucially, in order for $\tilde{\Xi}$ to be a symmetry of the nested Wilson loop, we must restrict to nested Wilson projectors $\tilde{P}(\mathbf{k})$ onto particle-hole conjugate pairs of Wilson bands, such that:

$$\begin{aligned}\tilde{\Xi}\tilde{P}(k_x,k_y,k_{z0})\tilde{\Xi}^{-1} &= \tilde{U}'(k_x,k_y,k_{z0})\tilde{P}^*(k_x,k_y,k_{z0})\tilde{U}'^{\dagger}(k_x,k_y,k_{z0})\\ &= \tilde{U}(k_x,k_y,k_{z0})\tilde{P}^*(k_x,k_y,k_{z0})\tilde{U}^{\dagger}(k_x,k_y,k_{z0}),\end{aligned} \tag{B15}$$

projects onto the same Wilson bands as $\tilde{P}(k_x,k_y,k_{z0})$, and where one can again take $\tilde{U}(k_x,k_y,k_{z0})=\mathbb{1}$ for spinless electrons without loss of generality. For the x-directed nested Wilson loop, $\tilde{\Xi}$ also does not change the direction of the product of projectors in Eq. (B9), and so the action of $\tilde{\Xi}$ (and thus $\mathcal{I}\times\mathcal{T}$) on $W_2(k_y)$ also follows simply from Eqs. (B10), (B12), and (B15):

$$\begin{aligned}\tilde{\Xi}W_{2(k_{x0},k_y,k_{z0})}\tilde{\Xi}^{-1} &= \tilde{\Xi}\tilde{V}(2\pi\hat{x})\tilde{\Pi}(k_{x0},k_y,k_{z0})\tilde{\Xi}^{-1}\\ &= \tilde{U}(k_{x0},k_y,k_{z0})\tilde{V}^*(2\pi\hat{x})\tilde{\Pi}^*(k_{x0},k_y,k_{z0})\tilde{U}^{\dagger}(k_{x0},k_y,k_{z0})\\ &= \tilde{U}(k_{x0},k_y,k_{z0})W^*_{2(k_{x0},k_y,k_{z0})}\tilde{U}^{\dagger}(k_{x0},k_y,k_{z0}).\end{aligned} \tag{B16}$$

The nested Wilson Hamiltonian is therefore invariant under an antiunitary particle-hole symmetry, which we denote as $\tilde{\tilde{\Xi}}$, that preserves the sign of k_y:

$$\tilde{\tilde{\Xi}}H_{W_2}(k_y)\tilde{\tilde{\Xi}}^{-1} = -\tilde{\tilde{U}}(k_y)H^*_{W_2}(k_y)\tilde{\tilde{U}}^{\dagger}(k_y), \tag{B17}$$

for which one can take $\tilde{\tilde{U}}(k_y)=\mathbb{1}$ for spinless electrons without loss of generality. Eq. (B17) implies that for every nested Wilson eigenstate $|\tilde{u}^n(k_{x0},k_y,k_{z0})\rangle$ with eigenvalue $\theta_2^n(k_y)$, there is another eigenstate with eigenvalue $-\theta_2^n(k_y)$:

$$\tilde{\tilde{\Xi}}|\tilde{u}^n(k_{x0},k_y,k_{z0})\rangle = \tilde{\tilde{U}}'(k_{x0},k_y,k_{z0})(|\tilde{u}^n(k_{x0},k_y,k_{z0})\rangle)^*, \tag{B18}$$

where $\tilde{\tilde{U}}'(k_{x0},k_y,k_{z0})$ is the product of $\tilde{\tilde{U}}(k_y)$ in Eq. (B17) and a $\mathbf{k}$-dependent unitary transformation that rotates the nested Wilson band index n, and is present for both spinful and spinless electrons. Taking the determinant of the right-hand side of Eq. (B16) and exploiting that $W_2(k_y)$ is invariant under $\tilde{\Xi}$:

$$\det(W_2(k_y)) = (\det(W_2(k_y)))^*, \tag{B19}$$

for both spinful and spinless electrons. Along with Eq. (B14), Eq. (B19) implies that at *all* values of k_y for which $W_2(k_y)$ is well-defined (*i.e.* there is a bulk and Wilson gap), $\det(W_2(k_z))$ is $\mathbb{Z}_2$ quantized:

$$\det(W_2(k_y)) = \pm 1, \tag{B20}$$

and thus also implies that the nested Berry phase $\gamma_2(k_y)$ is $\mathbb{Z}_2$ quantized:

$$\gamma_2(k_y) = 0,\pi. \tag{B21}$$

4. Higher-Order Topology in Gapped γ-XTe_2

In this section, we explicitly show that γ-$MoTe_2$, when gapped, is a noncentrosymmetric, non-symmetry-indicated HOTI. We begin with γ-$MoTe_2$, calculated with the structural parameters used in Ref. 64 (Fig. 6(a)). In the γ structure, $MoTe_2$ crystals are left invariant under the action of space group (SG) 31 in the nonstandard setting of $Pnm2_1$, which is generated by:

$$n_x = \left\{M_x\middle|0\frac{1}{2}\frac{1}{2}\right\},\ m_y = \left\{M_y\middle|000\right\},\ s_{2_1z} = \left\{C_{2z}\middle|0\frac{1}{2}\frac{1}{2}\right\}, \tag{B22}$$

as obtained from the GET GEN tool on the Bilbao Crystallographic Server[65]. Specifically, SG 31 is typically associated (and is listed for simplicity in the main text) with the standard symbol[66] $Pmn2_1$. However, because the standard symbol implies the (symmorphic) mirror reflection $m_x=\{M_x|000\}$, whereas the actual mirror symmetry in γ-$MoTe_2$ is $m_y=\{M_y|000\}$ (Eq. (B22)), then in this section we will use the more precise nonstandard symbol $Pnm2_1$ to characterize the structure of γ-$MoTe_2$ in SG 31. When the bulk band structure of γ-$MoTe_2$ is calculated with the

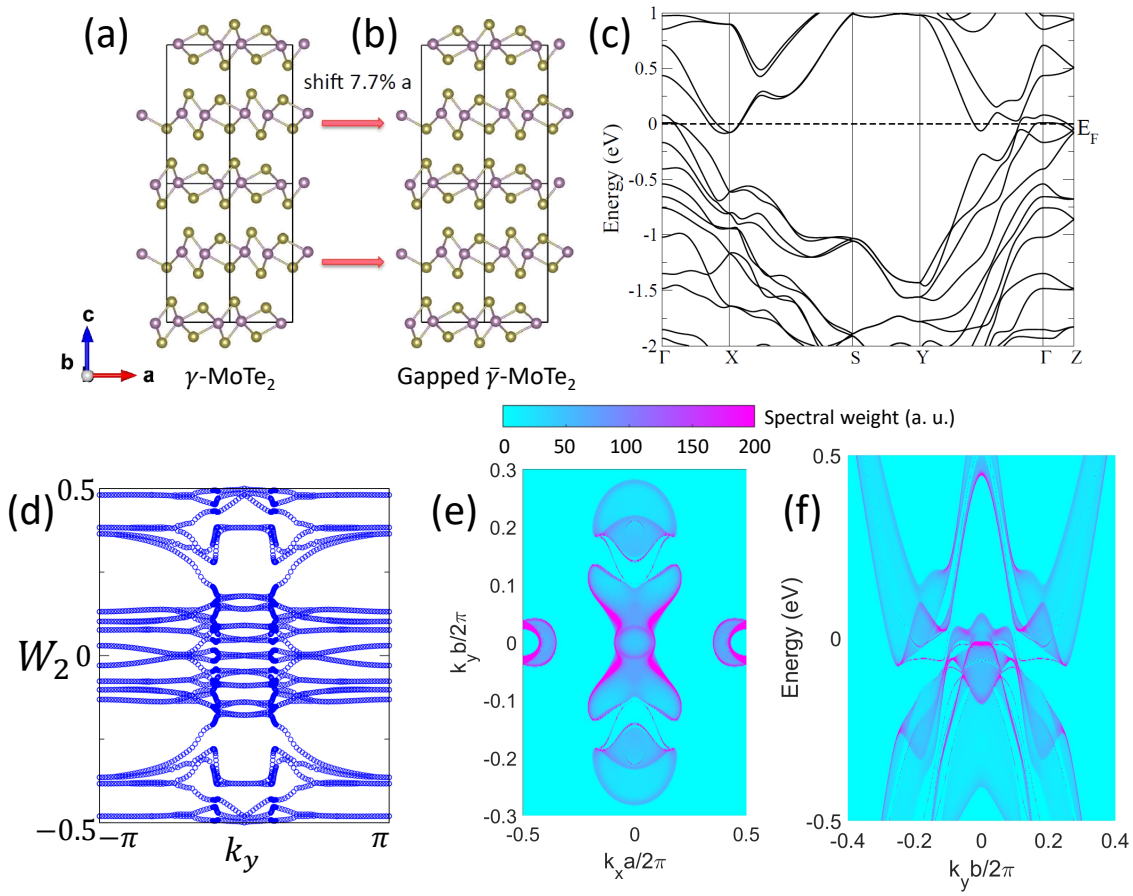

FIG. 6: (a) The crystal structure of γ-$MoTe_2$ (SG 31 in the nonstandard setting $Pnm2_1$, see text surrounding Eq. (B22)) in the type-II Weyl semimetal phase studied in Ref. 64. (b) By sliding alternating layers of $MoTe_2$ along the a-axis by $\sim 7.7\%$ of the a-direction lattice spacing, we realize an artificial centrosymmetric structure in SG 62 $Pnma$, which we designate as $\bar{\gamma}$-$MoTe_2$. The unstable $\bar{\gamma}$ structure coincides with the "T_0" structure of $MoTe_2$ introduced in Ref. 68 after the submission of this letter. (c) The bulk band structure of $\bar{\gamma}$-$MoTe_2$ is fully gapped, and exhibits the same parity eigenvalues as β-$MoTe_2$ (Table I and Fig. 2(d) of the main text). We then calculate the z-directed Wilson loop $W_1(k_x, k_y)$ of $\bar{\gamma}$-$MoTe_2$, which, like the Wilson spectrum of β-$MoTe_2$ (Fig. 3(c,d) of the main text) is gapped at $\theta_1 = \pm\pi/2$, indicating that $\bar{\gamma}$-$MoTe_2$ is a HOTI, and not a mirror TCI. (d) $W_2(k_y)$ of $\bar{\gamma}$-$MoTe_2$, calculated using the Wilson bands near $\theta_1 = 0$. As shown in Appendix B 3 a, $W_2(k_y)$ is Wilson particle-hole symmetric at each value at k_y due to the combined symmetry $\mathcal{I} \times \mathcal{T}$. By generalizing the arguments for $\mathcal{I}$- and rotation-symmetry-protected HOTIs introduced in Refs. 14,34,49, we conclude that the helical winding in (d) is representative of a strong topological phase enforced by $\mathcal{I}$ and $\mathcal{T}$ symmetries[50,52], in agreement with the bulk nontrivial $\mathbb{Z}_4$ parity index. As discussed in this section (Appendix B 4), this also implies that $W_2(k_z)$, which we found to be numerically difficult to calculate, must nevertheless be well-defined, and must also exhibit robust helical winding enforced by $\mathcal{I}$ and $\mathcal{T}$. Furthermore, the implied helical winding of $W_2(k_z)$ can alternatively be considered enforced by twofold screw and $\mathcal{T}$ symmetries[14,35], which are also symmetries of γ-$MoTe_2$, unlike $\mathcal{I}$ symmetry. Thus, $W_2(k_z)$ should continue to exhibit strong helical winding under a slight distortion from $\bar{\gamma}$-$MoTe_2$ back to a gapped γ-phase (the reverse of (a) and (b)). Therefore, gapped γ-$MoTe_2$ is a non-symmetry-indicated HOTI. (e) Spectral weight at the Fermi energy of states on the (001) surface of $\bar{\gamma}$-$MoTe_2$, calculated using the same methodology employed for Fig. 4(d,e) of the main text (Appendix B 1), and plotted as a function of the in-plane momenta $k_{x,y}$, and (f) along $k_x = 0$ as a function of energy. The surface states of $\bar{\gamma}$-$MoTe_2$ are gapped (f), and are nearly identical to the large, gapped, nontrivial, arc-like HOTI surface states of β-$MoTe_2$ (Fig. 4(d,e) of the main text). Because the surface states in (d,e) will remain gapped under infinitesimal distortion from $\bar{\gamma}$-$MoTe_2$ to gapped γ-$MoTe_2$, this provides further evidence that γ-$MoTe_2$ is a noncentrosymmetric, non-symmetry-indicated HOTI when gapped.

structural parameters used in Ref. 64, it exhibits tilted (type-II) Weyl points[64,67], and is thus semimetallic, and not insulating.

To gap the Weyl points, we slide alternating layers of γ-$MoTe_2$ along the a-axis by $\sim 7.7\%$ of the a lattice spacing

(Fig. 6(b)). After this distortion, the crystal develops an artificial, unstable centrosymmetry:

$$\mathcal{I} = \left\{ \mathcal{I} \middle| \frac{1}{2}\frac{1}{2}0 \right\}, \tag{B23}$$

and is thus characterized by SG 62 *Pnma*, a supergroup[66] of SG 31 $Pnm2_1$ that is generated by adding Eq. (B23) to the SG 31 generators in[65,66] Eq. (B22). The new, artificial structure in SG 62 *Pnma*, which we denote as $\bar{\gamma}$-$MoTe_2$ (Fig. 6(b)), coincides with the unstable "T_0" structure, which was introduced in Ref. 68 after the submission of this letter. Plotting the bulk band structure of $\bar{\gamma}$-$MoTe_2$ (Fig. 6(c)), we observe that all of the Weyl points along high symmetry lines have been removed. Furthermore, because nonmagnetic crystals in SG 62 *Pnma* host the combined symmetry $\mathcal{I} \times \mathcal{T}$, all of their bands are at least twofold degenerate, and hence cannot meet in conventional Weyl points along the lower-symmetry BZ planes and interior[69] not pictured in Fig. 6(c). Therefore, $\bar{\gamma}$-$MoTe_2$ is a bulk band insulator (though still metallic) at the Fermi energy.

Next, we diagnose the bulk topology of $\bar{\gamma}$-$MoTe_2$. The bulk bands exhibit all of the same parity eigenvalues as β-$MoTe_2$ (Table I and Fig. 2(d) of the main text). Thus, using the $\mathbb{Z}_4$ parity index developed in Refs. 35–38 and in the main text, $\bar{\gamma}$-$MoTe_2$ exhibits the strong indices of an $\mathcal{I}$- and $\mathcal{T}$-symmetric HOTI. We use Wilson loops to further determine that the mirror Chern numbers[70,71] of the y-directed mirrors are trivial in both the $k_y = 0, \pi$ planes. Specifically, we calculate the z-directed Wilson loop $W_1(k_x, k_y)$, using the 56 highest valence bands in energy, and find that it is gapped in the vicinity of $\theta_1 = \pm\pi/2$ at all values of $k_{x,y}$ (producing a Wilson spectrum similar to that of β-$MoTe_2$ shown in Fig. 3(c,d) of the main text), indicating that the y-directed mirror Chern numbers are trivial. Therefore, $\bar{\gamma}$-$MoTe_2$ is a HOTI, and not a TCI, as is also allowed by its bulk symmetry eigenvalues[35–37]. We further confirm the bulk topology by calculating the x-directed nested Wilson loop $W_2(k_y)$ of the separated grouping of Wilson bands near $\theta_1 = 0$ (Fig. 6(d)), employing the same numerical methods previously used for β-$MoTe_2$ (Appendix B 3). As shown Appendix B 3 a, $W_2(k_y)$ is Wilson particle-hole symmetric at each value of k_y due to the combined symmetry $\mathcal{I} \times \mathcal{T}$. We observe that $W_2(k_y)$ exhibits helical winding (Fig. 6(d)). Generalizing the arguments presented in Refs. 14,49 for rotation- and $\mathcal{I}$-protected HOTIs, band crossings in $W_1(k_x, k_y)$ can only manifest in Wilson particle-hole and $\mathcal{T}$-symmetric pairs, and thus the winding of $W_2(k_y)$ cannot be removed by a gap closure in the Wilson spectrum that is not accompanied by a gapless point in the energy spectrum. Therefore, the helical winding of $W_2(k_y)$ shown in Fig. 6(d) is indicative of a strong (higher-order) topological phase. A more rigorous $\mathcal{T}$-symmetric generalization of nested Berry phase will appear in Ref. 50.

Furthermore, in any $\mathcal{I}$- and $\mathcal{T}$-symmetric HOTI with gapped surface states and a large number of occupied bands[14], any nested Wilson loop, performed as prescribed in Appendix B 3, must exhibit helical winding. Therefore, $W_2(k_z)$, which we found numerically difficult to explicitly calculate due the more complicated forms of the x- and y-directed Wilson bands in $\bar{\gamma}$-$MoTe_2$, must nevertheless be well-defined, and display helical winding if correctly computed. Though it has not yet been explicitly demonstrated, we here outline how this winding can alternatively be interpreted as protected by the combination of twofold screw ($s_{2_1 z}$) and $\mathcal{T}$ symmetries, leaving the formal details for future works. In Refs. 14,15, it was shown that the combined magnetic symmetry of twofold rotation C_{2z} and $\mathcal{T}$ protects strong, odd-integer chiral winding of a nested Wilson loop $W_2(k_z)$ directed along the rotation axis (z-direction), and indicates that the bulk is a non-symmetry-indicated axion insulator. Because the simplest HOTI can be formed from superposing two time-reversed axion insulators[14,49], and because the irreducible (co)representations of C_{2z} and $s_{2_1 z}$ are closely related[27,66,72], then it is straightforward to argue that the presence of both $s_{2_1 z}$ and $\mathcal{T}$ symmetries in a 3D insulator can enforce helical winding of $W_2(k_z)$ that is indicative of strong, higher-order (crystalline) topology. Because γ-$MoTe_2$ is noncentrosymmetric, and thus cannot exhibit strong (nested) Wilson loop winding enforced by $\mathcal{I}$ symmetry, we will find this reasoning crucial for arguing that it nevertheless exhibits the bulk band-insulating topology of an $s_{2_1 z}$- and $\mathcal{T}$-protected HOTI.

To further support our diagnosis of $\bar{\gamma}$-$MoTe_2$ as a HOTI, we calculate the (001) surface states through surface Green's functions (Fig. 6(d,e)). Of the bulk crystal symmetries of SG 62 *Pnma* (Eqs. (B22) and (B23)), only M_y (as well as the rectangular lattice translations $T_{x,y}$) are preserved on the (001) surface. Therefore, the (001) surface of $\bar{\gamma}$-$MoTe_2$ respects wallpaper group[39,40,73] pm, which can only support twofold linear degeneracies at TRIM points and along the m_y-invariant BZ lines $k_y = 0, \pi$. Because the bulk $\mathbb{Z}_4$ invariant is even, then the strong Fu-Kane invariant is necessarily trivial[34–37,49], indicating that $\bar{\gamma}$-$MoTe_2$ is not a 3D TI, and does not host topological (unpaired) surface states at the (001) surface TRIM points. Next, because the surface states of $\bar{\gamma}$-$MoTe_2$, like those of β-$MoTe_2$, originate from bulk double band inversion at Γ (Fig. 6(c)), then mirror TCI cones[70,71] can only appear along $k_y = 0$, which coincides with the (001)-surface projection of Γ. In Fig. 6(e), we plot the (001) surface states of $\bar{\gamma}$-$MoTe_2$ at the Fermi energy, and observe the clear absence of mirror TCI cones along $k_y = 0$, in agreement with our earlier observation that the z-directed Wilson loop $W_1(k_x, 0)$ of $\bar{\gamma}$-$MoTe_2$ is gapped. We additionally calculate the surface states along $k_x = 0$ as a function of energy (Fig. 6(f)), further demonstrating that the (001) surface states of $\bar{\gamma}$-$MoTe_2$ are gapped, like those of β-$MoTe_2$ (Fig. 4(e) of the main text). This confirms, in agreement with the (nested) Wilson loop calculations

performed earlier in this section (Fig. 6(d)), that $\bar{\gamma}$-$MoTe_2$ is not a TCI, but is instead a HOTI with large, gapped surface states.

With these symmetry arguments established, and with the results of the (nested) Wilson loop and surface-state calculations in Fig. 6(c-e), we can finally exploit the previous diagnosis of $\bar{\gamma}$-$MoTe_2$ as a HOTI to diagnose the topology of gapped γ-$MoTe_2$. We model the transition away from the artifical $\bar{\gamma}$ structure by infinitesimally sliding back alternating layers of $MoTe_2$ along the a-axis (the reverse of the process depicted in Fig. 6(a,b)). This sliding lowers the crystal symmetry from SG 62 $Pnma$ back to SG 31 $Pnm2_1$, the SG of γ-$MoTe_2$. Because the sliding is infinitessimal, it does not close a bulk or surface gap, and therefore the bulk remains band insulating, and the (001) surface continues to exhibit large, nontrivial, gapped surface states. As shown in Ref. 35 using position-space symmetry arguments, nonmagnetic crystals in SG 31 $Pnm2_1$ can only host three kinds of topological surface or hinge states: the surface cones of a strong 3D TI, the surface cones of a mirror TCI, and the hinge states of an $s_{2_1 z}$- and $\mathcal{T}$-protected "rotation-anomaly"[14,35,74] TCI, which we consider to be a form of HOTI. Because $\bar{\gamma}$-$MoTe_2$ was previously determined to be neither a strong 3D TI nor a mirror TCI, and because we previously determined that its nested Wilson loop $W_2(k_z)$ must helically wind, then we conclude that gapped γ-$MoTe_2$ is a non-symmetry-indicated HOTI whose higher-order topology is protected by twofold screw and $\mathcal{T}$ symmetries. Furthermore, because the electronic and crystal structure of γ-WTe_2 is nearly identical to that of[75] γ-$MoTe_2$, then we conclude that γ-WTe_2, when gapped, is also a non-symmetry-indicated HOTI.

[1] W. Setyawan and S. Curtarolo, Computational Materials Science **49**, 299 (2010), ISSN 0927-0256, URL http://www.sciencedirect.com/science/article/pii/S0927025610002697.

[2] J. Ahn, D. Kim, Y. Kim, and B.-J. Yang, Phys. Rev. Lett. **121**, 106403 (2018), URL https://link.aps.org/doi/10.1103/PhysRevLett.121.106403.

[3] A. Bouhon and A. M. Black-Schaffer, ArXiv e-prints (2017), 1710.04871.

[4] T. c. v. Bzdušek and M. Sigrist, Phys. Rev. B **96**, 155105 (2017), URL https://link.aps.org/doi/10.1103/PhysRevB.96.155105.

[5] Y. Kim, B. J. Wieder, C. L. Kane, and A. M. Rappe, Phys. Rev. Lett. **115**, 036806 (2015), URL https://link.aps.org/doi/10.1103/PhysRevLett.115.036806.

[6] R. Yu, H. Weng, Z. Fang, X. Dai, and X. Hu, Phys. Rev. Lett. **115**, 036807 (2015), URL https://link.aps.org/doi/10.1103/PhysRevLett.115.036807.

[7] Y.-H. Chan, C.-K. Chiu, M. Y. Chou, and A. P. Schnyder, Phys. Rev. B **93**, 205132 (2016), URL https://link.aps.org/doi/10.1103/PhysRevB.93.205132.

[8] C. Fang, Y. Chen, H.-Y. Kee, and L. Fu, Phys. Rev. B **92**, 081201 (2015), URL https://link.aps.org/doi/10.1103/PhysRevB.92.081201.

[9] B. J. Wieder, Z. Wang, J. Cano, X. Dai, L. M. Schoop, B. Bradlyn, and B. A. Bernevig, arXiv e-prints arXiv:1908.00016 (2019), 1908.00016.

[10] M. Lin and T. L. Hughes, Phys. Rev. B **98**, 241103 (2018), URL https://link.aps.org/doi/10.1103/PhysRevB.98.241103.

[11] M. Ezawa, Phys. Rev. B **97**, 155305 (2018), URL https://link.aps.org/doi/10.1103/PhysRevB.97.155305.

[12] A. M. Essin, J. E. Moore, and D. Vanderbilt, Phys. Rev. Lett. **102**, 146805 (2009), URL https://link.aps.org/doi/10.1103/PhysRevLett.102.146805.

[13] N. Varnava and D. Vanderbilt, Phys. Rev. B **98**, 245117 (2018), URL https://link.aps.org/doi/10.1103/PhysRevB.98.245117.

[14] B. J. Wieder and B. A. Bernevig, ArXiv e-prints (2018), 1810.02373.

[15] J. Ahn and B.-J. Yang, Phys. Rev. B **99**, 235125 (2019), URL https://link.aps.org/doi/10.1103/PhysRevB.99.235125.

[16] *Python tight binding open-source package*, http://physics.rutgers.edu/pythtb/.

[17] L. Alvarez-Gaumé', S. Della Pietra, and G. Moore, Ann. Phys. **163**, 288 (1985).

[18] H. B. Nielsen and M. Ninomiya, Nucl. Phys. B **185**, 20 (1981).

[19] B. A. Bernevig, T. L. Hughes, and S.-C. Zhang, Science **314**, 1757 (2006), ISSN 0036-8075, URL http://science.sciencemag.org/content/314/5806/1757.

[20] A. Alexandradinata, X. Dai, and B. A. Bernevig, Physical Review B **89**, 155114 (2014).

[21] H. C. Po, H. Watanabe, and A. Vishwanath, Phys. Rev. Lett. **121**, 126402 (2018), URL https://link.aps.org/doi/10.1103/PhysRevLett.121.126402.

[22] J. Cano, B. Bradlyn, Z. Wang, L. Elcoro, M. G. Vergniory, C. Felser, M. I. Aroyo, and B. A. Bernevig, Phys. Rev. Lett. **120**, 266401 (2018), URL https://link.aps.org/doi/10.1103/PhysRevLett.120.266401.

[23] J. Cano, B. Bradlyn, L. Elcoro, Z. Wang, and B. A. Bernevig, *In Preparation*.

[24] A. Bouhon, A. M. Black-Schaffer, and R.-J. Slager, ArXiv e-prints (2018), 1804.09719.

[25] R. Jackiw and C. Rebbi, Phys. Rev. D **13**, 3398 (1976), URL https://link.aps.org/doi/10.1103/PhysRevD.13.3398.

[26] M. Pretko, Phys. Rev. B **96**, 035119 (2017), URL https://link.aps.org/doi/10.1103/PhysRevB.96.035119.

[27] B. Bradlyn, L. Elcoro, J. Cano, M. G. Vergniory, Z. Wang, C. Felser, M. I. Aroyo, and B. A. Bernevig, Nature **547**, 298 EP (2017), article, URL http://dx.doi.org/10.1038/nature23268.

[28] D. B. Litvin, *Magnetic Group Tables* (International Union of Crystallography, 2013), ISBN 978-0-9553602-2-0.
[29] J. Ahn, S. Park, and B.-J. Yang, Phys. Rev. X **9**, 021013 (2019), URL https://link.aps.org/doi/10.1103/PhysRevX.9.021013.
[30] W. A. Benalcazar, T. Li, and T. L. Hughes, Phys. Rev. B **99**, 245151 (2019), URL https://link.aps.org/doi/10.1103/PhysRevB.99.245151.
[31] Y. Hwang, J. Ahn, and B.-J. Yang, arXiv e-prints arXiv:1905.08128 (2019), 1905.08128.
[32] J. Langbehn, Y. Peng, L. Trifunovic, F. von Oppen, and P. W. Brouwer, Phys. Rev. Lett. **119**, 246401 (2017), URL https://link.aps.org/doi/10.1103/PhysRevLett.119.246401.
[33] L. Trifunovic and P. W. Brouwer, Phys. Rev. X **9**, 011012 (2019), URL https://link.aps.org/doi/10.1103/PhysRevX.9.011012.
[34] F. Schindler, Z. Wang, M. G. Vergniory, A. M. Cook, A. Murani, S. Sengupta, A. Y. Kasumov, R. Deblock, S. Jeon, I. Drozdov, et al., Nature Physics **14**, 918 (2018), ISSN 1745-2481, URL https://doi.org/10.1038/s41567-018-0224-7.
[35] Z. Song, T. Zhang, Z. Fang, and C. Fang, Nature Communications **9**, 3530 (2018), ISSN 2041-1723, URL https://doi.org/10.1038/s41467-018-06010-w.
[36] H. C. Po, A. Vishwanath, and H. Watanabe, Nature Communications **8**, 50 (2017), ISSN 2041-1723, URL https://doi.org/10.1038/s41467-017-00133-2.
[37] E. Khalaf, H. C. Po, A. Vishwanath, and H. Watanabe, Phys. Rev. X **8**, 031070 (2018), URL https://link.aps.org/doi/10.1103/PhysRevX.8.031070.
[38] E. Khalaf, Phys. Rev. B **97**, 205136 (2018), URL https://link.aps.org/doi/10.1103/PhysRevB.97.205136.
[39] B. J. Wieder, B. Bradlyn, Z. Wang, J. Cano, Y. Kim, H.-S. D. Kim, A. M. Rappe, C. L. Kane, and B. A. Bernevig, Science **361**, 246 (2018), ISSN 0036-8075, URL http://science.sciencemag.org/content/361/6399/246.
[40] B. J. Wieder and C. L. Kane, Phys. Rev. B **94**, 155108 (2016), URL http://link.aps.org/doi/10.1103/PhysRevB.94.155108.
[41] A. H. Castro Neto, F. Guinea, N. M. R. Peres, K. S. Novoselov, and A. K. Geim, Rev. Mod. Phys. **81**, 109 (2009), URL https://link.aps.org/doi/10.1103/RevModPhys.81.109.
[42] M. Fujita, K. Wakabayashi, K. Nakada, and K. Kusakabe, Journal of the Physical Society of Japan **65**, 1920 (1996), http://dx.doi.org/10.1143/JPSJ.65.1920, URL http://dx.doi.org/10.1143/JPSJ.65.1920.
[43] K. Nakada, M. Fujita, G. Dresselhaus, and M. S. Dresselhaus, Phys. Rev. B **54**, 17954 (1996), URL http://link.aps.org/doi/10.1103/PhysRevB.54.17954.
[44] P. Ruffieux, S. Wang, B. Yang, C. Sánchez-Sánchez, J. Liu, T. Dienel, L. Talirz, P. Shinde, C. A. Pignedoli, D. Passerone, et al., Nature **531**, 489 EP (2016), URL http://dx.doi.org/10.1038/nature17151.
[45] F. Zhang, Synthetic Metals **210**, 9 (2015), ISSN 0379-6779, reviews of Current Advances in Graphene Science and Technology, URL http://www.sciencedirect.com/science/article/pii/S0379677915300369.
[46] C. L. Kane and E. J. Mele, Phys. Rev. Lett. **95**, 146802 (2005), URL https://link.aps.org/doi/10.1103/PhysRevLett.95.146802.
[47] C. L. Kane and E. J. Mele, Phys. Rev. Lett. **95**, 226801 (2005), URL https://link.aps.org/doi/10.1103/PhysRevLett.95.226801.
[48] F. D. M. Haldane, Phys. Rev. Lett. **61**, 2015 (1988), URL https://link.aps.org/doi/10.1103/PhysRevLett.61.2015.
[49] F. Schindler, A. M. Cook, M. G. Vergniory, Z. Wang, S. S. P. Parkin, B. A. Bernevig, and T. Neupert, Science Advances **4** (2018), URL http://advances.sciencemag.org/content/4/6/eaat0346.
[50] F. Schindler, S. S. Tsirkin, T. Neupert, B. A. Bernevig, and B. J. Wieder, *In Preparation*.
[51] B. Bradlyn, Private communication.
[52] B. J. Wieder, A. Gromov, and B. Bradlyn, *In Preparation*.
[53] P. E. Blöchl, Phys. Rev. B **50**, 17953 (1994), URL https://link.aps.org/doi/10.1103/PhysRevB.50.17953.
[54] G. Kresse and D. Joubert, Phys. Rev. B **59**, 1758 (1999), URL https://link.aps.org/doi/10.1103/PhysRevB.59.1758.
[55] G. Kresse and J. Hafner, Phys. Rev. B **47**, 558 (1993), URL https://link.aps.org/doi/10.1103/PhysRevB.47.558.
[56] G. Kresse and J. Furthmller, Computational Materials Science **6**, 15 (1996), ISSN 0927-0256, URL http://www.sciencedirect.com/science/article/pii/0927025696000080.
[57] J. P. Perdew, K. Burke, and M. Ernzerhof, Phys. Rev. Lett. **77**, 3865 (1996), URL https://link.aps.org/doi/10.1103/PhysRevLett.77.3865.
[58] Inorganic Crystal Structure Database (ICSD) (Fachinformationszentrum Karlsruhe, Karlsruhe, Germany, 2015).
[59] B. E. Brown, Acta Crystallographica **20**, 268 (1966), URL https://onlinelibrary.wiley.com/doi/abs/10.1107/S0365110X66000513.
[60] I. Souza, N. Marzari, and D. Vanderbilt, Phys. Rev. B **65**, 035109 (2001), URL https://link.aps.org/doi/10.1103/PhysRevB.65.035109.
[61] W. A. Benalcazar, B. A. Bernevig, and T. L. Hughes, Science **357**, 61 (2017), ISSN 0036-8075, URL http://science.sciencemag.org/content/357/6346/61.
[62] W. A. Benalcazar, B. A. Bernevig, and T. L. Hughes, Phys. Rev. B **96**, 245115 (2017), URL https://link.aps.org/doi/10.1103/PhysRevB.96.245115.
[63] A. Alexandradinata, Z. Wang, and B. A. Bernevig, Physical Review X **6**, 021008 (2016).
[64] Z. Wang, D. Gresch, A. A. Soluyanov, W. Xie, S. Kushwaha, X. Dai, M. Troyer, R. J. Cava, and B. A. Bernevig, Physical Review Letters **117**, 056805 (2016), URL http://link.aps.org/doi/10.1103/PhysRevLett.117.056805.
[65] A. M. Ilia, P.-M. J. Manuel, C. Cesar, K. Eli, I. Svetoslav, M. Gotzon, K. Asen, and W. Hans, *zkri* (2006), vol. 221, chap. Bilbao Crystallographic Server: I. Databases and crystallographic computing programs, p. 15, 1, URL https://www.

degruyter.com/view/j/zkri.2006.221.issue-1/zkri.2006.221.1.15/zkri.2006.221.1.15.xml.
[66] C. J. Bradley and A. P. Cracknell, *The Mathematical Theory of Symmetry in Solids* (Clarendon Press Oxford, Oxford, United Kingdom, 1972), ISBN 0199582580.
[67] A. A. Soluyanov, D. Gresch, Z. Wang, Q. Wu, M. Troyer, X. Dai, and B. A. Bernevig, Nature **527**, 495 (2015), ISSN 1476-4687, URL https://www.nature.com/articles/nature15768.
[68] F.-T. Huang, S. J. Lim, S. Singh, J. Kim, L. Zhang, J.-W. Kim, M.-W. Chu, K. M. Rabe, D. Vanderbilt, and S.-W. Cheong, arXiv e-prints arXiv:1908.03082 (2019), 1908.03082.
[69] O. Vafek and A. Vishwanath, Ann. Rev. Condensed Matter Phys. **5**, 83 (2014).
[70] J. C. Y. Teo, L. Fu, and C. L. Kane, Phys. Rev. B **78**, 045426 (2008), URL https://link.aps.org/doi/10.1103/PhysRevB.78.045426.
[71] T. H. Hsieh, H. Lin, J. Liu, W. Duan, A. Bansil, and L. Fu, Nature Communications **3**, 982 EP (2012), article, URL http://dx.doi.org/10.1038/ncomms1969.
[72] L. Elcoro, B. Bradlyn, Z. Wang, M. G. Vergniory, J. Cano, C. Felser, B. A. Bernevig, D. Orobengoa, G. de la Flor, and M. I. Aroyo, Journal of Applied Crystallography **50**, 1457 (2017), URL https://doi.org/10.1107/S1600576717011712.
[73] S. M. Young and B. J. Wieder, Phys. Rev. Lett. **118**, 186401 (2017), URL https://link.aps.org/doi/10.1103/PhysRevLett.118.186401.
[74] C. Fang and L. Fu, ArXiv e-prints (2017), 1709.01929.
[75] H.-J. Kim, S.-H. Kang, I. Hamada, and Y.-W. Son, Phys. Rev. B **95**, 180101 (2017), URL https://link.aps.org/doi/10.1103/PhysRevB.95.180101.